inorganics

MDPI

Article

Synergistic Effect of Co and Mn Co-Doping on SnO₂ Lithium-Ion Anodes

Adele Birrozzi [1,2,†], Angelo Mullaliu [1,2,†], Tobias Eisenmann [1,2], Jakob Asenbauer [1,2], Thomas Diemant [1,2], Dorin Geiger [3], Ute Kaiser [3], Danilo Oliveira de Souza [4], Thomas E. Ashton [5], Alexandra R. Groves [5], Jawwad A. Darr [5], Stefano Passerini [1,2] and Dominic Bresser [1,2,*]

[1] Helmholtz Institute Ulm (HIU), Helmholtzstrasse 11, 89081 Ulm, Germany; adele.birrozzi@kit.edu (A.B.); angelo.mullaliu@kit.edu (A.M.); tobias.eisenmann@kit.edu (T.E.); jakob.asenbauer@kit.edu (J.A.); thomas.diemant@uni-ulm.de (T.D.); stefano.passerini@kit.edu (S.P.)
[2] Karlsruhe Institute of Technology (KIT), P.O. Box 3640, 76021 Karlsruhe, Germany
[3] Central Facility for Electron Microscopy, Ulm University, Albert-Einstein-Allee 11, 89081 Ulm, Germany; dorin.geiger@uni-ulm.de (D.G.); ute.kaiser@uni-ulm.de (U.K.)
[4] Elettra-Sincrotrone Trieste, 34012 Basovizza, Italy; danilo.oliveiradesouza@elettra.eu
[5] Department of Chemistry, University College London (UCL), London WC1H 0AJ, UK; t.ashton@ucl.ac.uk (T.E.A.); alexandra.groves.17@ucl.ac.uk (A.R.G.); j.a.darr@ucl.ac.uk (J.A.D.)
* Correspondence: dominic.bresser@kit.edu
† These authors contributed equally to this work.

Abstract: The incorporation of transition metals (TMs) such as Co, Fe, and Mn into SnO₂ substantially improves the reversibility of the conversion and the alloying reaction when used as a negative electrode active material in lithium-ion batteries. Moreover, it was shown that the specific benefits of different TM dopants can be combined when introducing more than one dopant into the SnO₂ lattice. Herein, a careful characterization of Co and Mn co-doped SnO₂ via transmission electron microscopy coupled with energy-dispersive X-ray spectroscopy and X-ray diffraction including Rietveld refinement is reported. Based on this in-depth investigation of the crystal structure and the distribution of the two TM dopants within the lattice, an ex situ X-ray photoelectron spectroscopy and ex situ X-ray absorption spectroscopy were performed to better understand the de-/lithiation mechanism and the synergistic impact of the Co and Mn co-doping. The results specifically suggest that the antithetical redox behaviour of the two dopants might play a decisive role for the enhanced reversibility of the de-/lithiation reaction.

Keywords: SnO₂; transition metal doping; reaction mechanism; anode; lithium battery

1. Introduction

The development of high-performance electrochemical energy storage systems providing high energy and high power density is one of the cornerstones towards the transition to renewable energy sources. At present, lithium-ion batteries (LIBs) are the technology of choice in this regard, especially for portable electronic devices and (hybrid) electric vehicles [1,2]. The state-of-the-art active material for the negative electrode is graphite, owing to its high theoretical specific capacity of 372 mAh g⁻¹ and its very low de-/lithiation potential, yielding high energy densities at the full-cell level. However, further improvement of graphite as an active material appears limited and the rather slow kinetics of the lithium intercalation reaction hinder the fast charging of the resulting LIBs [3,4]. Thus, several alternative anode materials have been studied in recent years, which can be roughly classified by the underlying lithium storage mechanism, including insertion, alloying, conversion, and more recently a combined conversion and alloying process [5].

Alloying anode materials such as Si and Sn provide very high specific capacities up to 993 mAh g⁻¹ (Sn) or even 3578 mAh g⁻¹ (Si). Nonetheless, these very high capacities are accompanied by extensive volume variation upon cycling, reaching up to about 300% [6].

Pure conversion-type materials such as transition metal oxides also provide specific capacities up to about 1000 mAh g^{-1}, but they suffer from a rather high de-/lithiation potential, a pronounced voltage hysteresis for the lithiation and delithiation process and commonly limited cycling stability [7–9]. Lately, the combination of these two material classes in one, also referred to as conversion-alloying materials (CAMs), gained increasing interest [5]. Such CAMs as, for instance, TM-doped ZnO, GeO$_2$, or SnO$_2$, provide superior specific capacity, energy density, and energy efficiency compared with pure conversion-type materials [10–13], while the volume variation is significantly suppressed compared with pure alloying compounds [14]. The key towards such superior performance is the introduction of the TM, as this limits the aggregation of the alloying domains and provides an electronically conductive network throughout the initial particle [15–17]. The latter is important to enable the reversible formation of Li$_2$O, which presumably aids the buffering of the volume variation. The choice of the TM dopant, however, is important as well, since this has an effect on the rate capability, reactivity with the electrolyte, cycling stability, and energy density in full cells [10,13,16]. In the case of TM-doped SnO$_2$, for instance, the introduction of Mn is favoured when it comes to energy density, while Co, for instance, enables a better cycling stability and rate capability [10]. In order to benefit from both, the authors have very recently developed co-doped SnO$_2$ that was prepared by a readily scalable continuous hydrothermal synthesis method [18]. Following a carbon coating, the best performing co-doped SnO$_2$, i.e., Sn$_{0.9}$Co$_{0.05}$Mn$_{0.05}$O$_2$ (SCMO), showed very good performance in half-cells and SCMO‖LiNi$_{0.5}$Mn$_{1.5}$O$_4$ full cells with a non-optimized specific energy of 312 Wh kg^{-1} (based on the mass of the two active materials) and an energy efficiency of 86%.

Herein, we report an in-depth investigation of the underlying mechanism and the synergistic impact of the two dopants by ex situ X-ray photoelectron spectroscopy (XPS) and ex situ X-ray absorption spectroscopy (XAS), following a careful characterization of the material via transmission electron microscopy (TEM) coupled with energy-dispersive X-ray spectroscopy (EDX) and X-ray diffraction (XRD), including Rietveld refinement. In particular, the results show that the antithetical redox behaviour of Co and Mn plays a decisive role for enhanced performance.

2. Result and Discussion

2.1. General Properties of (Carbon-Coated) Sn$_{0.9}$Co$_{0.05}$Mn$_{0.05}$O$_2$

Sn$_{0.9}$Co$_{0.05}$Mn$_{0.05}$O$_2$ (SCMO) and carbon-coated Sn$_{0.9}$Co$_{0.05}$Mn$_{0.05}$O$_2$ (SCMO@C), with a carbon content of 16 wt% as revealed by thermogravimetric analysis (TGA), were first characterized by TEM (Figure 1). Both materials are composed of rod-shaped, single-crystalline nanoparticles with a length and diameter in the range of 25–30 and 5–8 nm, respectively. Two interlayer distances were identified (0.262 and 0.334 nm), corresponding to the (101) and (110) planes in the rutile SnO$_2$ structure, respectively. Regarding SCMO@C, an amorphous carbon layer of around 3–5 nm was observed on the nanoparticles, as highlighted by the orange arrows and lines in Figure 1c,d, forming a percolating network among the single particles.

The homogeneous distribution of carbon was corroborated by the additionally performed EDX mapping (Figure 2). However, an EDX analysis also revealed that a cavity in the centre of the nanoparticle agglomerate showed a higher carbon concentration, indicating that the initial cavity was "filled" with carbon. More importantly, EDX mapping showed that the two dopants Co and Mn were homogeneously dispersed in the sample along with Sn. The EDX analysis also provided an estimation of the TM contents: For Co, the calculated value of about 0.051 (referring to the substitution of Sn in Sn$_{1-x-y}$Co$_x$Mn$_y$O$_2$, i.e., x for Co; note that we do not consider the oxygen vacancies in this formula as the result of the aliovalent TM doping) is in good agreement with the expected concentration with regard to the initial metal ratio of the precursors (also considering the experimental error of this method), while it is a little lower for Mn with about 0.032 (i.e., y in Sn$_{1-x-y}$Co$_x$Mn$_y$O$_2$). This might indicate that the incorporation of Co into the SnO$_2$ structure is slightly favoured compared with Mn.
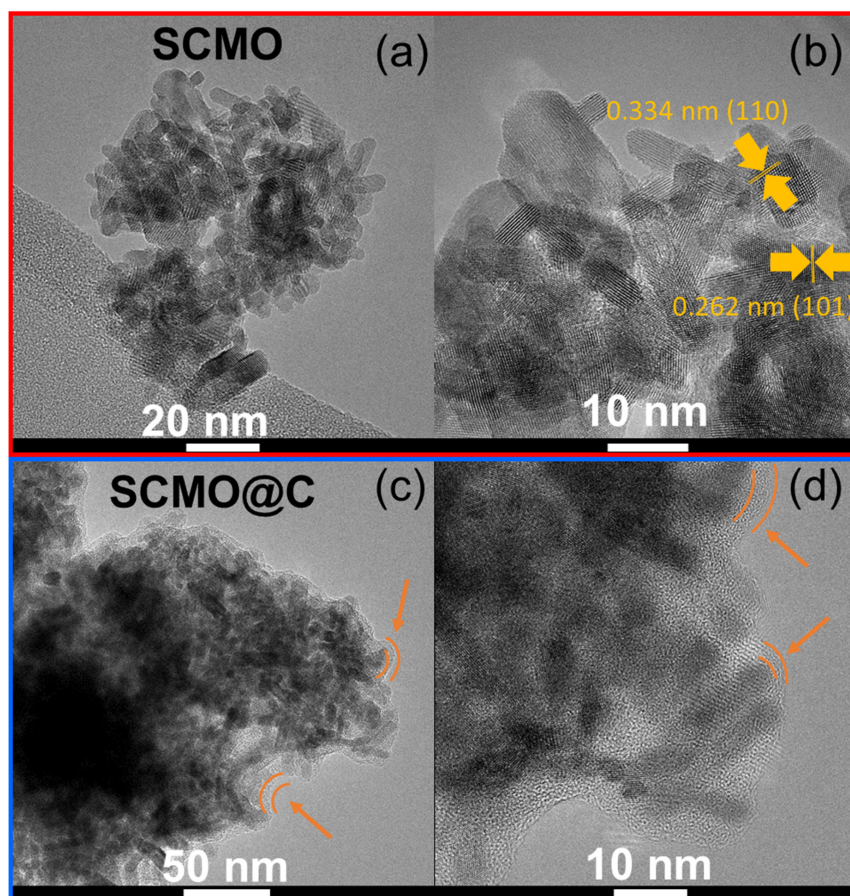
Figure 1. Transmission electron micrographs of (**a**,**b**) SCMO and (**c**,**d**) SCMO@C at different magnifications. The yellow lines in (**b**) highlight the lattice fringes of (110) and (101) planes; orange lines and arrows in (**c**,**d**) indicate an amorphous carbon layer on the nanoparticle surface.

Figure 2. EDX analysis of SCMO@C with the corresponding high-angle annular dark-field (HAADF) image shown in the top left and the elemental mapping for Sn in pink, Co in yellow, C in red (the cavity filled with carbon is highlighted by a white circle), O in blue, and Mn in green.

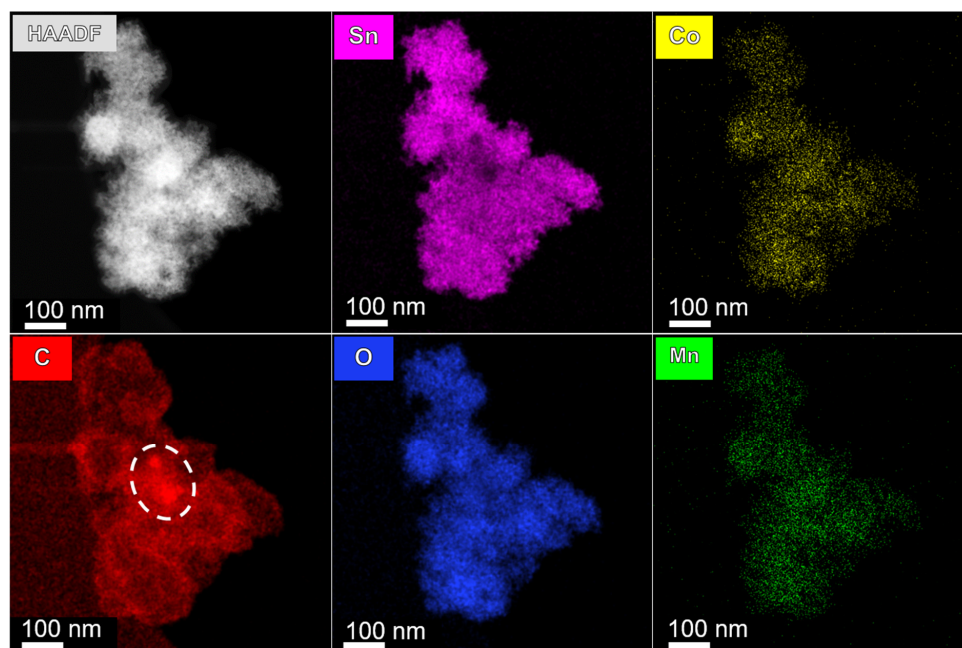Thereafter, XRD data were collected and Rietveld refinements undertaken. The two fitted XRD patterns for SCMO and SCMO@C are displayed in Figure 3. The starting structural model for the refinement is presented in Table S1 and an overview of the results is provided in Table S2. For the refinement, both TMs were assumed to dope the SnO_2 structure and replace the Sn atoms in the *2a* Wyckoff site. Nonetheless, this assumption cannot be confirmed by the Rietveld analysis due to the small concentration of the two dopants, requiring additional insights from the X-ray Absorption Spectroscopy (XAS) investigation, which will be discussed later. Generally, both XRD patterns are characterized by rather broad reflections, indicating the nanocrystalline nature of the two materials. According to the fitting, the domain (i.e., crystallite) size was in the range from 6 (equatorial) to 11 (axial) nm (see Table S2), which is in fairly good agreement with the TEM data (Figure 1), confirming the observation of single-crystalline, elongated nanoparticles. Besides, the good overlap of the structural parameters, atomic positions, and atomic occupancies renders the two materials essentially equivalent.
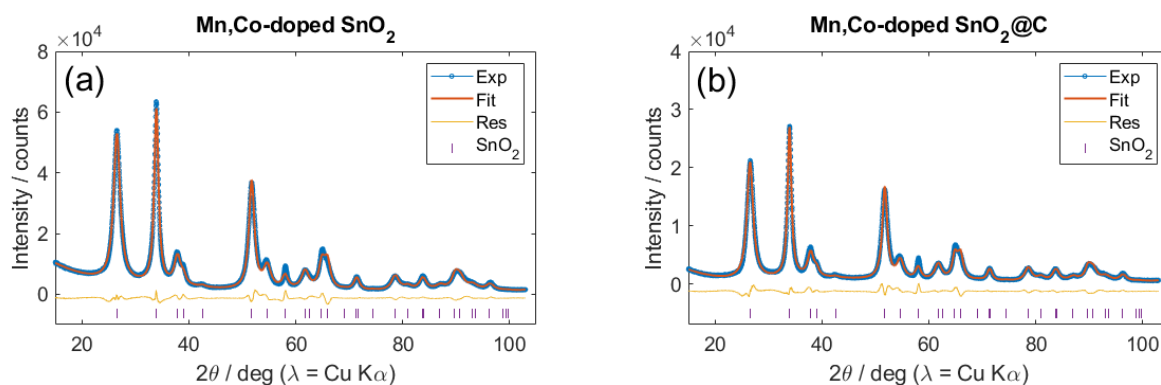

Figure 3. XRD patterns and the corresponding Rietveld refinement for (**a**) SCMO and (**b**) SCMO@C. Each panel contains the experimental pattern, the Rietveld refinement, the residual curve, and the expected reflections for the SnO_2 phase (PDF 01-070-6995).

A very minor difference was found for the unit cell volume, which slightly expanded for the carbon-coated material by 0.1%. Given the great overlap of the other values, this might be related to a minor reduction in the TM dopants as a result of the carbon coating procedure, as observed previously for TM-doped ZnO [19], and the corresponding increase in the ionic radius. Nevertheless, this increase was essentially negligible, thus, it was not expected to have a great impact on the de-/lithiation mechanism. Another outcome of the Rietveld refinement concerned the stoichiometry of the two materials. Following the independent refinement of SCMO and SCMO@C by constraining the sum of the metals' (Sn, Mn, Co) occupancies (*Occ*) to unity and forcing the *Occ*(Mn) value to be the same as *Occ*(Co) to avoid undesirable fluctuations in the fit, the best fit was obtained for the composition $[MnCo]_{0.05}Sn_{0.95}O_2$. This finding was generally in line with the EDX data, indicating that the eventual composition contained less TMs than expected from the precursor ratio. Nonetheless, it must be kept in mind that the EDX analysis revealed a relatively lower Mn concentration compared with Co. Hence, the actual composition was presumably in the range from 0.025 to 0.05 for Co and in the range from 0.025 to 0.032 for Mn. This was further corroborated by the XAS data (see below), specifically the K-edge absorbance step recorded for Mn and Co. The comparison of the experimentally determined and the calculated values (Table S3) showed that the experimental values were in-between the two theoretical compositions of $Sn_{0.95}Co_{0.025}Mn_{0.025}O_2$ and $Sn_{0.9}Co_{0.05}Mn_{0.05}O_2$, though somewhat closer to the lower TM content.

2.2. Ex Situ XPS

In the next step, an ex situ XPS analysis, was conducted to gain insights into the reaction mechanism. XPS measurements were carried out on electrodes in the pristine, fully

lithiated and fully delithiated state, and on one electrode subjected to 10 cycles (in the fully delithiated state) for Sn, and on electrodes in the pristine state for Mn and Co. The Mn2p and Co2p spectra of the pristine electrode are presented in Figure 4.
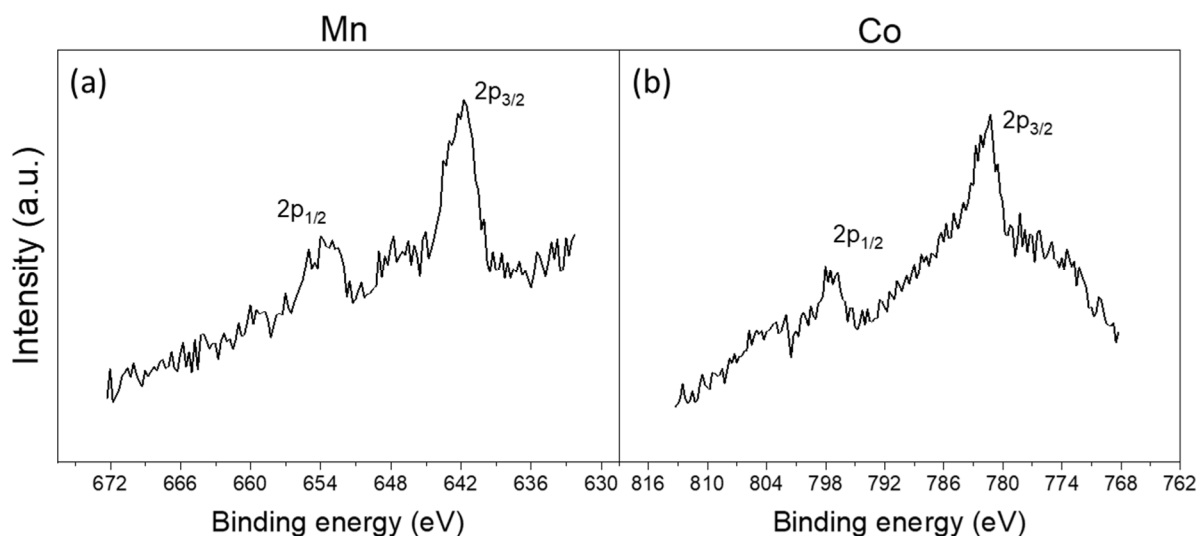

Figure 4. XPS detail spectra in the (**a**) Mn2p and (**b**) Co2p region.

Prior to the discussion of the results it appears noteworthy that the peaks of transition metals with unpaired electrons (such as Mn^{2+} to Mn^{4+} as well as Co^{2+} and Co^{3+}) show a complicated multiplet splitting due to coupling effects during the photo-ionization [20]. We therefore refrained from a peak fit for these two elements. In both cases, a main peak doublet was observed: in the Mn2p region (Figure 4a) the peaks were detected at ~642 eV ($Mn2p_{3/2}$) and 654 eV ($Mn2p_{1/2}$), in the Co2p region (Figure 4b) they were found at ~782 eV ($Co2p_{3/2}$) and 797 eV ($Co2p_{1/2}$). No major satellite peaks were observed in both cases. The observed peak positions are typical for Mn in an oxidation state of +3 or +4 and for Co in an oxidation state of +2 or +3, respectively [21]. In the case of Mn, a differentiation between these states is not possible based on the binding energy (BE) alone. For Co, however, the absence of major satellite peaks points to the predominant presence of Co^{3+}, since prominent satellites are usually observed only for Co^{2+}, but not for Co^{3+} [20]. An analysis of the Mn and Co data obtained for the cycled electrodes was not feasible, unfortunately, since the peak intensities in the Mn2p and Co2p region were below the detection limit for all cycled samples, presumably owing to the low concentration of the two elements.

In contrast, the Sn3d peaks were detected for all samples (Figure 5). Essentially, the XPS results are in good agreement with the previous analysis. For the pristine electrode (Figure 5a), the position of the Sn3d peak doublet at 487.4 (Sn $3d_{5/2}$) and 495.8 eV (Sn $3d_{3/2}$) indicates the presence of Sn^{4+} [21–23]. For the fully lithiated sample at 0.01 V (Figure 5b), a significant reduction in the peak intensity indicates the formation of a surface layer on the active material particles, assigned to the formation of the solid electrolyte interphase (SEI). Additionally, a significant shift of the $Sn3d_{5/2}$ peak position to 482.1 eV was observed, i.e., a BE even lower than that of metallic Sn^0 (~485 eV) [21]. This low BE can be explained by the formation of a LiSn alloy, in which negative charge is transferred from the Li to the Sn atoms [24,25]. Two peak doublets were detected for the delithiated sample at 3.0 V (Figure 5c). The one of lower intensity at lower binding energy ($Sn3d_{5/2}$ peak at 484.8 eV) can be assigned to metallic Sn, while the other one ($Sn3d_{5/2}$ peak at 487.0 eV), with a substantially higher intensity, is related to an oxidized Sn species, presumably Sn^{4+}. The sample after 10 cycles shows in principle a similar picture with two peak doublets (Figure 5d); however, the one assigned to the oxidized Sn species shifted by 1 eV to a lower BE ($Sn3d_{5/2}$ peak at 486.0 eV), which might indicate the presence of Sn^{2+} in this sample. In both cases, the contribution from metallic tin is rather small, having less than 20% of the total intensity. Nonetheless, the finding that not all Sn was fully reoxidized is in good

agreement with a very recent study on transition metal-doped zinc oxide, for which the same behaviour was observed [16].
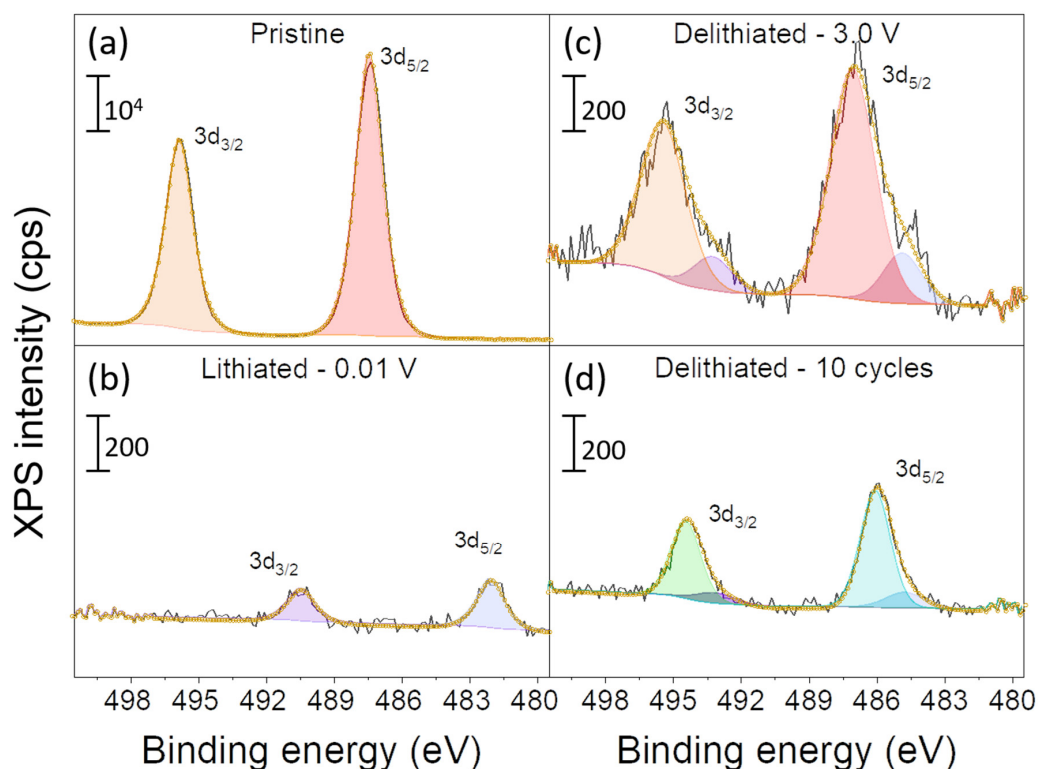

Figure 5. XPS detail spectra in the Sn3d region recorded for (**a**) a pristine electrode, (**b**) at the fully lithiated state (0.01 V), as well as (**c**,**d**) at the fully delithiated state (3.0V) (**c**) after one cycle and (**d**) after 10 cycles.

2.3. Ex Situ XAS—Experimental Data

Due to the lithiation-induced loss of the long-range crystalline ordering [10], the greater sampling depth compared with XPS (several nm for XPS versus several μm for XAS), and the low concentration of the two dopants, synchrotron XAS (with its high sensitivity and brilliance) is the method of choice to follow the evolution of the electronic and local structure of CAMs. Thus, XAS can provide valuable insights into the reaction mechanism and the role of the TM dopants. In Figure 6, the typical first-cycle dis-/charge profile of SCMO@C in half-cell configuration is shown, including the different cut-off potentials for the ex situ XAS investigation.

The X-ray absorption near edge structure (XANES) spectra recorded at the different states of charge for the Sn L_3-edge as well as the Co and Mn K-edge are presented in Figure 7. The spectra at the Sn L_3-edge were collected in transmission mode and are divided into two panels, i.e., Figure 7a,b, for the sake of clarity. Figure 7a displays the evolution of the Sn L_3-edge spectra during the first discharge, i.e., lithiation, while in Figure 7b the spectra recorded upon the first charge and after 10 cycles are presented (in both cases also the spectrum of the pristine electrode is provided for a direct comparison). Upon discharge, Sn was reduced to the metallic state at 0.6 V and formed an alloy with lithium at lower potentials, i.e., at 0.2 V and 0.01 V, with an increasing lithium content at lower potentials, which was in good agreement with the ex situ XPS data. A more in-depth analysis and discussion of the data is provided in the next section, along with the ab initio calculations. During the charge, tin was reversibly re-oxidized. A comparison of the Sn L_3-edge spectra recorded at 0.2 V upon discharge and charge revealed essentially the same spectral features (Figure S1). Further delithiation to 3.0 V (Figure 7b) yielded tetravalent tin as in the pristine state. The broadening of the spectral features was assigned to the

electrochemical conversion and alloying reaction, which had a substantial impact on the crystal structure [10], while also a partially incomplete reoxidation, as indicated by the ex situ XPS analysis, might contribute to this broadening. Accordingly, the (further broadened) spectrum obtained for the electrodes subjected to 10 full dis-/charge cycles and recovered at 3.0 V showed the reoxidation to tetravalent tin, at least to a large extent.
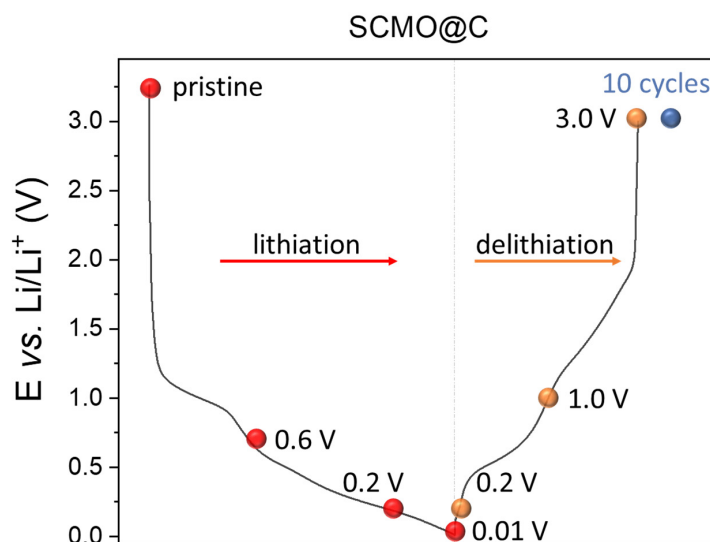

Figure 6. Dis-/charge profile of SCMO@C-based electrodes in half-cell configuration with an indication of the different cut-off potentials for the ex situ XAS investigation.
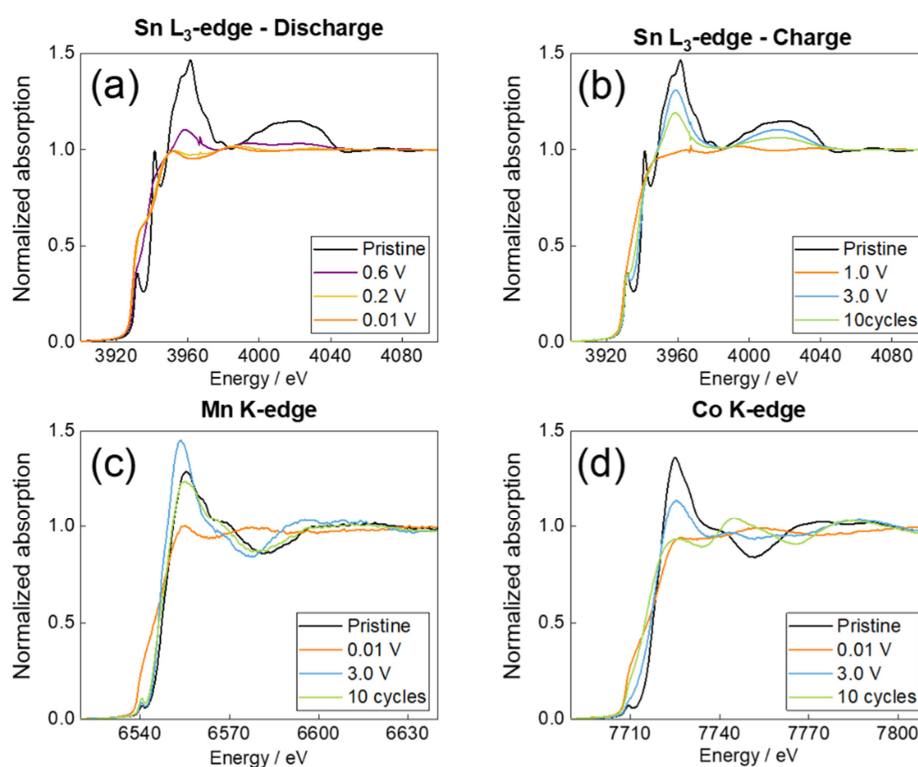
Figure 7. (**a**,**b**) Ex situ XANES spectra recorded at the Sn L_3-edge during (**a**) discharge (0.6 V, 0.2 V, and 0.01 V) and (**b**) charge (1.0 V, 3.0 V, and after 10 cycles at 3.0 V). Both panels include also the spectrum recorded for the pristine electrode for direct comparison. (**c**,**d**) Ex situ XANES spectra recorded at the (**c**) Mn K-edge and (**d**) Co K-edge, including the spectra of the pristine electrode as well as the electrodes discharged to 0.01 V and re-charged to 3.0 V after one complete cycle and 10 cycles.

Complementary information concerning the electrochemical reaction was revealed by the Mn and Co K-edge ex situ XANES spectra (Figure 7c,d, recorded in fluorescence mode due to the low TM concentrations). In Figure 7c, the evolution of the Mn K-edge from the pristine state to the fully discharged state (0.01 V) and back to the fully charged state (3.0 V) and the fully charged state after 10 cycles is depicted. The same plot is shown for the Co K-edge in Figure 7d. In the pristine state, both TMs were located in *2a* Wyckoff sites, replacing Sn in the rutile SnO_2 structure. The spectra of the fully discharged electrodes (0.01 V) confirmed the presence of metallic Mn and Co, suggesting the complete reduction in both TM dopants. This finding was confirmed by analysing the extended X-ray absorption fine structure (EXAFS) data (Figure S2). Upon charging, both TMs were reoxidized at 3.0 V, which was still the case on charging after 10 cycles. The local environment, however, changed after cycling, as apparent from the differing spectral features compared with the pristine state, indicating that the two TMs appeared to form other oxides with distinct structural environments. A more detailed analysis of the local coordination, though, is difficult due to the very low signal-to-noise ratio of the EXAFS data (Figure S3). Nevertheless, the ab initio XANES simulation of some Mn- and Co-based oxides provides further insights into the possible compounds formed upon cycling, as discussed in the following.

2.4. Ex Situ XAS—Comparison of Experiment and Simulation

Figure 8 compares simulated spectra (by the finite difference method near edges structure (FDMNES)) with the experimentally obtained ones. The pristine spectra recorded at the Sn L_3-edge, Mn K-edge, and Co K-edge are displayed in Figure 8a–c, respectively. The Sn L_3-edge spectrum was simulated by simply considering pure SnO_2 regarding the low dopant concentration. For the Mn and Co K-edge spectra, a small fraction of Sn in SnO_2 was replaced with Mn or Co to mimic the doping. The thus obtained simulated spectra were in good agreement with the corresponding experimental data, which also confirmed that doping of the two TMs into the SnO_2 structure was successful.
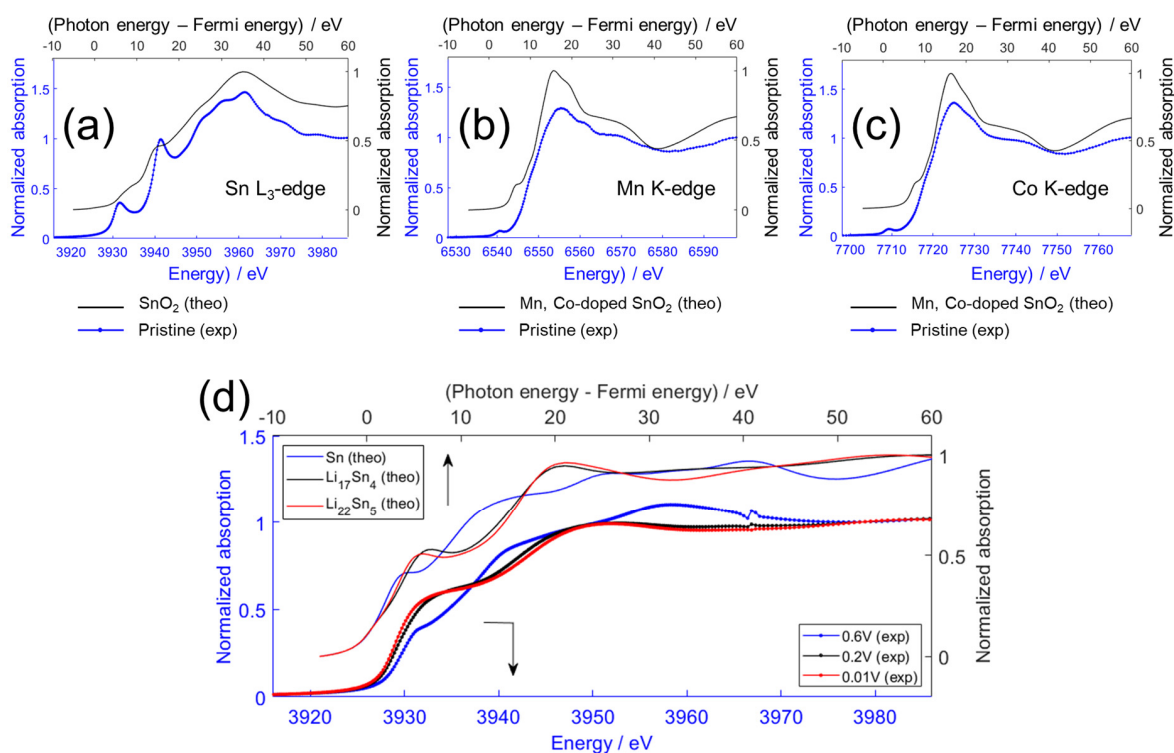

Figure 8. Comparison of the experimental and simulated XANES spectra: (**a**) Sn L_3-edge of the pristine sample; (**b**) Mn K-edge of the pristine sample; (**c**) Co K-edge of the pristine sample; (**d**) Sn L_3-edge of the ex situ samples discharged to 0.6 V, 0.2 V, and 0.01 V.

In Figure 8d, the experimental Sn L_3-edge spectra recorded for the ex situ samples discharged to 0.6 V, 0.2 V and 0.01 V are compared with the calculated spectra. The Sn L_3-edge spectrum calculated for metallic Sn was in good agreement with the experimental spectrum of the electrode discharged to 0.6 V, indicating that the conversion reaction was essentially complete at this potential and that Sn was fully reduced to the metallic state. At lower potentials, the subsequent alloying reaction occurred, as confirmed by the ex situ spectra obtained for the electrodes discharged to 0.2 V and 0.01 V. The small difference between the two spectra is sufficient to assign a distinct LiSn alloy to each state of a charge: simulated data for $Li_{17}Sn_4$ was a good match to the Sn L_3-edge observed experimentally at 0.2 V, while $Li_{22}Sn_5$ matched well with the experimental spectrum of the sample discharged to 0.01 V. Indeed, taking a closer look revealed that the calculated spectra can also describe the slightly dissimilar absorptions around 3930, 3942, and 3960 eV, further corroborating the suggestion of different Li/Sn ratios of 4.25 and 4.4 at 0.2 V and 0.01 V, respectively. This finding is of particular interest, as there was some discussion in the past about whether $Li_{22}Sn_5$ [26–28] or $Li_{17}Sn_4$ [29] is the maximum lithium concentration alloy that can be obtained electrochemically. The results suggest that both phases can be obtained, one after the other, upon discharge to sufficiently low potentials.

To gain additional insights into the reaction mechanism of Mn and Co co-doped SnO_2 and unveil the impact of the two dopants, the experimental XANES spectra were compared with ab initio simulated XANES spectra (Figure 9). The spectral features of the ex situ samples discharged to 0.01 V were in reasonable agreement with the XANES spectra calculated for metallic Mn (Figure 9a) and metallic Co (Figure 9b). The broadening of the spectral features in the experimental spectrum presumably originated from the highly disordered nature of the electrochemically formed metallic Mn and Co, when lithiating SCMO, which was different from the standard references used to calculate the XANES spectra. This also explained the slightly different modulation of the signal after the main edge, plausibly resulting from the deformation of the coordination shells (see also Figure S2 and the corresponding discussion).

The interpretation of the experimental Mn K-edge (Figure 9c) and Co K-edge (Figure 9d) spectra recorded for the ex situ samples charged to 3.0 V (after the first discharge and after 10 cycles) is more complex. These spectra were presumably showing a mixture of different oxide species that were not easily discernible. Therefore, XANES spectra of several reference oxides were calculated and compared with the experimental ones. At the Mn K-edge (Figure 9c), the 3.0 V ex situ data resembled the theoretical spectrum calculated for MnO with regard to the edge position and spectral shape, suggesting that the re-oxidation was not fully reversible. In contrast, the ex situ samples recovered after 10 cycles appeared to be a closer match to the Mn_2O_3 reference data. This observation suggests that the oxidation state of Mn increased upon cycling from approximately (+2) to (+3). A similar observation was reported earlier for manganese silicate, indicating that Mn might be generally prone to such behaviour upon continuous cycling when setting the upper cut-off potential to 3.0 V [30]. The comparison with the calculated MnO_2 XANES spectrum and the rather different spectral features also suggests that Mn did not reach a formal oxidation state of (+4) upon cycling under the given conditions.

The evolution of the experimental Co K-edge spectra showed the opposite trend. In this case, the ex situ sample recovered after 10 cycles, featured a lower energy edge position than the ex situ sample and recovered after the first charge to 3.0 V, implying that the oxidation state of Co decreased upon cycling; in other words, the reoxidation became less reversible. Based on the edge position, the Co-based oxide after the 1st charge may have a partially trivalent character (the experimental spectrum resembled Co_3O_4), similar to the pristine state, while the oxidation state after 10 cycles was closer to (+2).
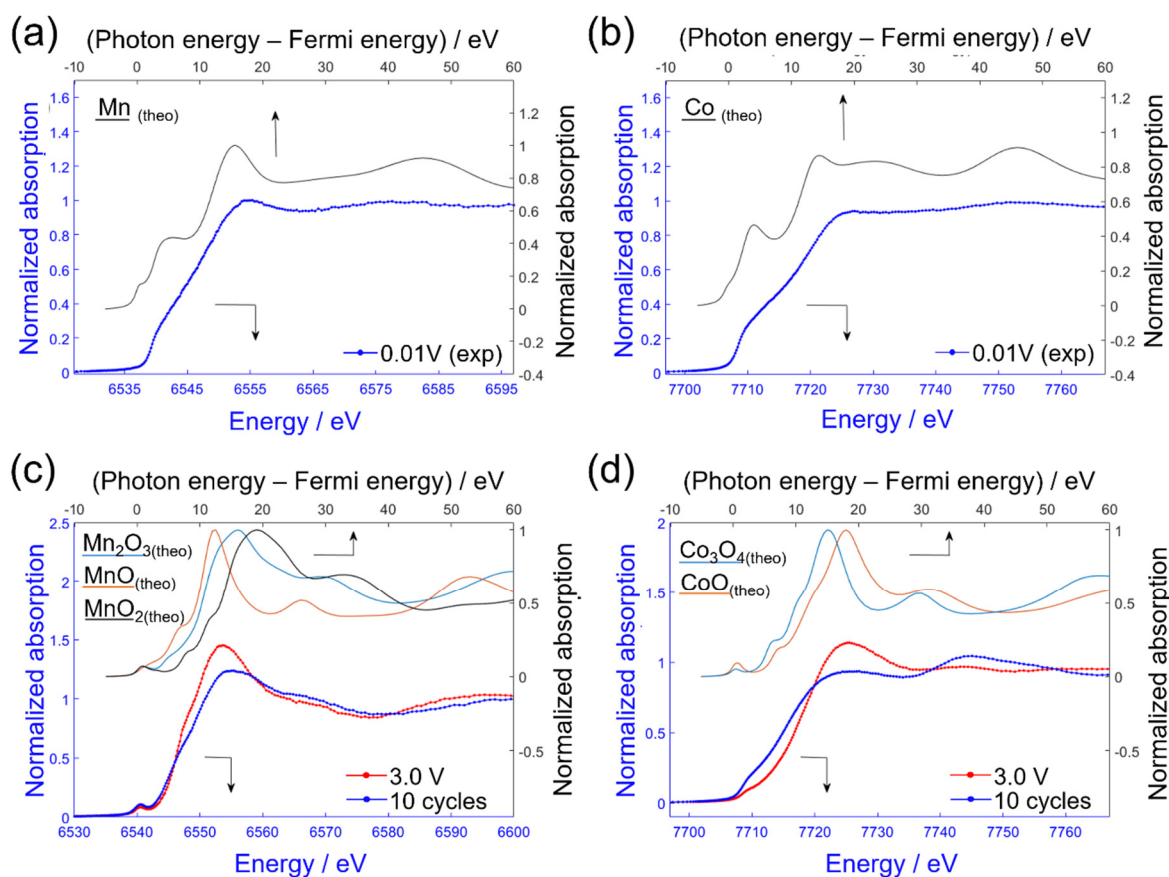
Figure 9. (**a**,**b**) Comparison of the experimental and calculated XANES spectra at (**a**) the Mn K-edge and (**b**) Co K-edge at 0.01 V. In both cases the experimental XANES spectra are compared with theoretical XANES spectra calculated for metallic Mn or Co. (**c**,**d**) Comparison of the experimental XANES spectra recorded for the ex situ samples charged to 3.0 V and after 10 cycles at the (**c**) Mn K-edge and the (**d**) Co K-edge with theoretical XANES spectra calculated for various manganese and cobalt oxide references, i.e., MnO, Mn_2O_3, and MnO_2 as well as CoO and Co_3O_4, respectively.

This intriguing finding of opposite trends concerning the reoxidation upon cycling may provide an explanation for the synergistic effect of the two dopants, resulting in the superior cycling stability reported earlier [18], since the loss in capacity owing to the decreasing reoxidation of cobalt may have been balanced by the increasing reoxidation of manganese.

3. Conclusions

The careful characterisation of SnO_2 nanoparticles (co-doped with Mn and Co) was accomplished using several complementary methods, including TEM coupled with EDX, Rietveld-refined XRD, XAS, and XPS. The results showed that both TM dopants were homogeneously distributed within the material and replaced Sn in *2a* Wyckoff sites. The dopant concentration, however, was slightly lower than expected from the initial precursor ratio in the hydrothermal flow process. A subsequent ex situ XPS and ex situ XAS study coupled with ab initio XANES simulations allows the investigation of the role of the two dopants for the de-/lithiation mechanism. In fact, the low amount of the two dopants rendered XAS as a highly suitable analytical method due to its high atomic sensitivity. The ex situ spectra for electrodes dis-/charged to selected cut-off potentials revealed a comprehensive understanding of the de-/lithiation mechanism; at 0.6 V, the conversion reaction appeared complete, while the alloying reaction of Li and Sn occurred at lower potentials. Two different LiSn alloys were identified; $Li_{17}Sn_4$ at 0.2 V and $Li_{22}Sn_5$ at 0.01 V. Moreover, tin oxide was reversibly re-formed to a great extent upon charge, even after

10 cycles. Additionally, the conversion of the doping elements to the corresponding metals upon discharge and their reoxidation during charge was confirmed. The comparison of the experimental and simulated XANES spectra, furthermore, allowed initial insights to be gained into the manganese and cobalt oxide species formed. While the average oxidation state for manganese in the fully de-lithiated state increased approximately from (+2) to (+3) upon cycling, cobalt experienced the reversed trend, with a decreasing oxidation state from a mix of (+2/+3) after the first cycle to mainly (+2) after 10 cycles. These results enabled an enhanced understanding of the reaction mechanism of this TM-doped SnO_2 and related conversion-alloying materials in general, and Mn and Co co-doped SnO_2 in particular. Therefore, this work will support the development of new and sustainable lithium-ion anode materials with greater reversibility and stability.

4. Materials and Methods

4.1. Synthesis of (Carbon-Coated) $Sn_{0.9}Co_{0.05}Mn_{0.05}O_2$

The synthesis of $Sn_{0.9}Co_{0.05}Mn_{0.05}O_2$ (SCMO) was reported in detail in a previous publication [18]. In brief, aqueous solutions of cobalt(II) nitrate hexahydrate (99%, Merck, Darmstadt, Germany), manganese(II) nitrate tetrahydrate (98%, Merck, Darmstadt, Germany), and potassium stannate (K_2SnO_3) trihydrate (99%, Merck, Darmstadt, Germany) were prepared. These solutions were fed into a continuous hydrothermal flow synthesis reactor [31] in stoichiometric amounts, whereupon the reaction with superheated deionized water at 450 °C under highly turbulent mixing conditions, produced an aqueous nanoparticle product stream that was cooled and recovered continuously from the process at atmospheric pressure and 40 °C. The resulting slurry was cleaned via dialysis in deionized water, followed by freeze-drying to yield the targeted SCMO nanoparticles. For the subsequent carbon coating, the SCMO powder was dispersed in an aqueous glucose (Thermofisher, Waltham, MA, USA) solution with an active material/glucose ratio of 1:1.5. The mixture was heated to 180 °C overnight in a stainless steel autoclave (Berghof, Eningen, Germany) under continuous stirring. Afterwards, the solid product was washed several times with deionized water via centrifugation and dried at 80 °C overnight. Eventually, the product was manually ground to obtain a fine powder and calcined in a tubular furnace (Nabertherm, Lilienthal, Germany) at 500 °C for 4 h under argon (heating rate: 3 K min^{-1}).

4.2. Physicochemical Characterization

TEM and EDX measurements were carried out using a Thermofisher Talos 200X TEM (Thermofisher, Waltham, MA, USA) equipped with a SuperX EDX detector operating at 200 kV. TGA was performed using a TA Instruments Q5000 under O_2 atmosphere in the temperature range from room temperature to 600 °C (heating rate: 3 K min^{-1}). The powder XRD characterization was performed using a Bruker D8 Advance (Bruker, Billerica, MA, USA) equipped with a Cu K_α radiation source (λ = 0.15406 nm) in a Bragg-Brentano geometry. The XRD patterns were recorded in the range from 20° to 120° in 2θ, with a step size of 0.03° and a 10 s/point acquisition time. Rietveld refinement was conducted using the GSAS-II software [32]. The starting structural model is reported in Table S1. The instrumental parameters were obtained from a LaB_6 standard; accordingly, the instrumental broadening parameters, i.e., U, V, W, X, and Y, were kept fixed to 4.397 $\times$ 10^{-4} deg^2, -5.720×10^{-4} deg^2, 2.577 $\times$ 10^{-4} deg^2, 1.855 $\times$ 10^{-2} deg, and 2 $\times$ 10^{-5} deg, respectively. The peak shape was refined with a uniaxial isotropic particle size broadening model (*(101)* reflection as unique axis) and by optimizing the respective parameters, i.e., the equatorial and axial size. The scale factor, background, sample displacement, unit cell parameters, peak shape, and atomic parameters were refined in the given order.

4.3. Ex Situ X-ray Photoelectron Spectroscopy

The (cycled) electrodes used for the ex situ XPS experiments were prepared by mixing the SCMO active material (75 wt%), conductive carbon (20 wt%, Super C65, Imerys, Paris, France), and the binder (5 wt%, sodium carboxymethyl cellulose, CMC, Dow Wolff Cellu-

losics, Bomlitz, Germany) for 2 h in zirconia jars using a planetary ball mill (Pulverisette 4, Fritsch, Idar-Oberstein, Germany). Firstly, the CMC was dissolved in deionized water. When the CMC was completely dissolved, the conductive carbon and SCMO were added. The resulting slurry was cast on dendritic copper current collector (battery grade, Schlenk, Roth, Germany) with a wet film thickness of 150 μm. Once the slurry was completely dry, disks with a diameter of 12 mm were cut and dried overnight at 120 °C under vacuum. The electrodes were then transferred into an argon-filled glove box for the cell assembly using Swagelok®-type T-cells. Polyethylene fleeces (Freudenberg, Weinheim, Germany) were used as separators and drenched with 1M LiPF$_6$ in a 1:1 mixture of ethylene carbonate (EC) and dimethyl carbonate (DMC) as electrolyte (UBE). After cycling the cells were disassembled in the glove box and the electrodes were recovered and washed with 150 μL of DMC (UBE, Minato, Japan) to remove the remaining electrolyte. Subsequently, the electrodes were dried and transferred to the XPS chamber in an air-tight sample transfer-box to avoid surface contamination and contact with the ambient atmosphere. The XPS measurements were acquired on a PHI 5800 MultiTechnique ESCA System (Physical Electronics, Feldkirchen, Germany), using monochromatized Al K$_\alpha$ radiation (300 W, 15 kV), a detection angle of 45°, and pass energies at the analyser of 93.9 and 29.35 eV for the survey and detail spectra, respectively. For the binding energy calibration, the main C1s peak of the conductive carbon additive (and adventitious carbon) was set to 284.8 eV. The spectra in the Sn3d region were analysed by a peak fit using the CasaXPS software, applying Shirley-type backgrounds and a Gaussian-Lorentzian mixed peak shape. Both the intensity ratio (3:2) and the spin-orbit splitting (8.4 eV) of the Sn3d peak doublets were set to the expected values [21].

4.4. Ex Situ X-ray Absorption Spectroscopy—Sample Preparation

For the ex situ XAS study, electrodes were prepared analogously to the ex situ XPS samples by mixing the SCMO active material (75 wt%), conductive carbon (20 wt%, Super C65, Imerys, Paris, France), and the binder (5 wt%, sodium carboxymethyl cellulose, CMC, Dow Wolff Cellulosics, Bomlitz, Germany) for 2 h in zirconia jars using a planetary ball mill (Pulverisette 4, Fritsch, Idar-Oberstein, Germany). Firstly, the CMC was dissolved in deionized water. Once the CMC was completely dissolved, the conductive carbon and SCMO were added. In this case, however, the resulting slurry was cast on carbon paper (TM Carbon Paper (TP-030), Toray, Chūō, Giappone) using a laboratory-scale doctor blade. Two sets of electrodes were prepared: for one, the wet-film thickness was set to 150 μm, and for the other one, the wet-film thickness was set to 300 μm. Subsequently, the electrodes were dried overnight at room temperature. Next, disc-shaped electrodes with a diameter of 12 mm were punched and dried overnight under vacuum at 120 °C. The final mass loading of the electrodes was ca. 2 and 5 mg cm^{-2} for the first and second set, respectively. The different active material mass loading was needed to obtain sufficient absorption at all three metal edges, i.e., the Co and Mn K-edges as well as the Sn L$_3$-edge. All electrodes were cycled in three-electrode Swagelok-type cells (assembled in an argon-filled glove box, MBraun, Garching, Germany) with lithium metal foil (battery grade, Honjo, Osaka, Japan) serving as counter and reference electrodes. A GF/D Whatman glass fibre sheet was used as the separator and soaked with the electrolyte, i.e., 1M LiPF$_6$ in a 1:1 mixture of ethylene carbonate (EC) and dimethyl carbonate (DMC) supplied by UBE (Minato, Japan). The cells were cycled to varying cut-off potentials (see also Figure 4) and disassembled in an argon-filled glove box with a H$_2$O and O$_2$ level of less than 0.01 ppm. The cycled electrodes were rinsed with DMC, dried under argon atmosphere in the glove box, and sealed in polyethylene (PE) foils to avoid any contact with the ambient atmosphere. For the standard compounds serving as references for the data analysis, the corresponding materials were mixed with cellulose (cellulose powder, Thermofisher, Waltham, USA) and pressed into pellets.

4.5. Ex Situ X-ray Absorption Spectroscopy—Data Collection

The XAS experiments were conducted at the XAFS beamline at the Elettra synchrotron in Trieste, Italy. The beamline was designed to cover a wide energy range from 2.4 to 27.0 keV, allowing the analysis of both TMs and Sn. The beamline setup comprises three ionization chambers filled with argon/helium/nitrogen in an optimized ratio for achieving maximum absorption in each chamber. The storage ring operated at 2.0 GeV in top-up mode with a typical current of 309 mA. The samples were analysed in transmission and fluorescence mode at the K-edge for Co and Mn and in transmission mode at the L_3-edge for Sn. For all measurements, an internal reference (e.g., the corresponding metal foil) were measured as well in order to calibrate the energy upon consecutive scans. No drifts of the energy scale were observed during the experiment. The energy selection of the synchrotron beam was made by using a fixed exit monochromator, equipped with a pair of Si(111) crystals. The spectra at the Co and Mn K-edges were collected with a constant k-step of 0.03 Å^{-1} with a 5 s/point acquisition time. Data were collected in the range from 7414 to 8500 eV for the Co K-edge, from 6244 to 7100 eV for the Mn K-edge, and from 3634 to 4150 eV for the Sn L_3-edge. The step and acquisition time were the same as for the TMs. All data were calibrated and pre-analysed using the Athena software within the Demeter package [33].

4.6. Ab Initio XANES Simulation

The ab initio simulation of the XANES spectra was performed using the FDMNES code [34]. The Sn L_3-edge, Mn K-edge, and the Co K-edge were calculated in the photo-electron energy range $-5 < E < 60$ eV with respect to the Fermi energy level. The L_3-edge threshold was calculated with the finite difference method (FDM), while the multiple scattering theory (MST) was used for the K-edge thresholds. The Hedin-Lundqvist complex potential [35] was used to calculate the excited states. The absorption cross-section was calculated within the dipolar approximation. Clusters of 5 Å built around each non-equivalent absorbing atom were considered. The space group symmetry was taken into account and the convolution parameters were kept constant for all spectra.

4.7. Extended X-ray Absorption Fine Structure Analysis

The EXAFS analysis was performed with the GNXAS package [36,37] based on the MST theory. Only the spectra attributable to the metallic species were analysed because of the rather low signal-to-noise ratio. The experimental EXAFS spectra were fitted with four relevant contributions by including three two-body ($\gamma^{(2)}$) term signals and one three-body ($\gamma^{(3)}$) term signal, following a fitting procedure reported earlier [38].

Supplementary Materials: The following are available online at https://www.mdpi.com/article/10.3390/inorganics10040046/s1, Figure S1: Comparison of the Sn L3-edge X-ray absorption spectra of the SCMO@C-based electrodes discharged (in red) and charged (in black) to 0.2 V; Figure S2: EXAFS analysis of the Mn and Co K-edge data obtained for the fully lithiated state of the SCMO@C-based electrode (0.01 V); Figure S3: EXAFS signal at the Mn (left) and Co (right) K-edge for the pristine SCMO@C-based electrode and the ex situ samples charged to 3.0 V in the first cycle and after 10 cycles, Table S1: Starting structural model for SnO2 that was used for the Rietveld refinement of the XRD data recorded for SCMO and SCMO@C: Graphical representation of the structure and main structural information (Occ = occupancy); Table S2: Results of the Rietveld refinement and the applied constraints. The values given in brackets indicate the error; Table S3: Comparison of the experimental Mn and Co K-edge absorbance edge step with values that were calculated for a composition of $Sn_{0.9}Co_{0.05}Mn_{0.05}O_2$ and $Sn_{0.95}Co_{0.025}Mn_{0.025}O_2$, following the results of the Rietveld refinement of the XRD data, the EDX data, and the initial precursor ratio. The experimental values were recorded in transmission mode.

References

1. Armand, M.; Axmann, P.; Bresser, D.; Copley, M.; Edström, K.; Ekberg, C.; Guyomard, D.; Lestriez, B.; Novák, P.; Petranikova, M.; et al. Lithium-Ion Batteries—Current State of the Art and Anticipated Developments. *J. Power Sources* **2020**, *479*, 228708. [CrossRef]
2. Armand, M.; Tarascon, J.-M. Building Better Batteries. *Nature* **2008**, *451*, 652–657. [CrossRef] [PubMed]
3. Asenbauer, J.; Eisenmann, T.; Kuenzel, M.; Kazzazi, A.; Chen, Z.; Bresser, D. The Success Story of Graphite as a Lithium-Ion Anode Material—Fundamentals, Remaining Challenges, and Recent Developments Including Silicon (Oxide) Composites. *Sustain. Energy Fuels* **2020**, *4*, 5387–5416. [CrossRef]
4. Xu, K.; Lam, Y.; Zhang, S.S.; Jow, T.R.; Curtis, T.B. Solvation Sheath of Li$^+$ in Nonaqueous Electrolytes and Its Implication of Graphite/Electrolyte Interface Chemistry. *J. Phys. Chem. C* **2007**, *111*, 7411–7421. [CrossRef]
5. Bresser, D.; Passerini, S.; Scrosati, B. Leveraging Valuable Synergies by Combining Alloying and Conversion for Lithium-Ion Anodes. *Energy Environ. Sci.* **2016**, *9*, 3348–3367. [CrossRef]
6. Obrovac, M.N.; Chevrier, V.L. Alloy Negative Electrodes for Li-Ion Batteries. *Chem. Rev.* **2014**, *114*, 11444–11502. [CrossRef] [PubMed]
7. Bresser, D.; Paillard, E.; Niehoff, P.; Krueger, S.; Mueller, F.; Winter, M.; Passerini, S. Challenges of "Going Nano": Enhanced Electrochemical Performance of Cobalt Oxide Nanoparticles by Carbothermal Reduction and In Situ Carbon Coating. *ChemPhysChem* **2014**, *15*, 2177–2185. [CrossRef] [PubMed]
8. Cabana, J.; Monconduit, L.; Larcher, D.; Palacín, M.R. Beyond Intercalation-Based Li-Ion Batteries: The State of the Art and Challenges of Electrode Materials Reacting Through Conversion Reactions. *Adv. Mater.* **2010**, *22*, E170–E192. [CrossRef] [PubMed]
9. Fang, S.; Bresser, D.; Passerini, S. Transition Metal Oxide Anodes for Electrochemical Energy Storage in Lithium- and Sodium-Ion Batteries. *Adv. Energy Mater.* **2020**, *10*, 1902485. [CrossRef]
10. Ma, Y.; Ma, Y.; Giuli, G.; Diemant, T.; Behm, R.J.; Geiger, D.; Kaiser, U.; Ulissi, U.; Passerini, S.; Bresser, D. Conversion/Alloying Lithium-Ion Anodes—Enhancing the Energy Density by Transition Metal Doping. *Sustain. Energy Fuels* **2018**, *2*, 2601–2608. [CrossRef]
11. Asenbauer, J.; Varzi, A.; Passerini, S.; Bresser, D. Revisiting the Energy Efficiency and (Potential) Full-Cell Performance of Lithium-Ion Batteries Employing Conversion/Alloying-Type Negative Electrodes. *J. Power Sources* **2020**, *473*, 228583. [CrossRef]
12. Asenbauer, J.; Binder, J.R.; Mueller, F.; Kuenzel, M.; Geiger, D.; Kaiser, U.; Passerini, S.; Bresser, D. Scalable Synthesis of Microsized, Nanocrystalline $Zn_{0.9}Fe_{0.1}$O-C Secondary Particles and Their Use in $Zn_{0.9}Fe_{0.1}$O-C/$LiNi_{0.5}Mn_{1.5}O_4$ Lithium-Ion Full Cells. *ChemSusChem* **2020**, *13*, 3504–3513. [CrossRef] [PubMed]
13. Eisenmann, T.; Asenbauer, J.; Rezvani, S.J.; Diemant, T.; Behm, R.J.; Geiger, D.; Kaiser, U.; Passerini, S.; Bresser, D. Impact of the Transition Metal Dopant in Zinc Oxide Lithium-Ion Anodes on the Solid Electrolyte Interphase Formation. *Small Methods* **2021**, *5*, 2001021. [CrossRef] [PubMed]
14. Asenbauer, J.; Kuenzel, M.; Eisenmann, T.; Birrozzi, A.; Chang, J.-K.; Passerini, S.; Bresser, D. Determination of the Volume Changes Occurring for Conversion/Alloying-Type Li-Ion Anodes upon Lithiation/Delithiation. *J. Phys. Chem. Lett.* **2020**, *8*, 8238–8245. [CrossRef]
15. Mueller, F.; Geiger, D.; Kaiser, U.; Passerini, S.; Bresser, D. Elucidating the Impact of Cobalt Doping on the Lithium Storage Mechanism in Conversion/Alloying-Type Zinc Oxide Anodes. *ChemElectroChem* **2016**, *3*, 1311–1319. [CrossRef]
16. Trapananti, A.; Eisenmann, T.; Giuli, G.; Mueller, F.; Moretti, A.; Passerini, S.; Bresser, D. Isovalent vs. Aliovalent Transition Metal Doping of Zinc Oxide Lithium-Ion Battery Anodes—In-Depth Investigation by Ex Situ and Operando X-Ray Absorption Spectroscopy. *Mater. Today Chem.* **2021**, *20*, 100478. [CrossRef]

17. Asenbauer, J.; Passerini, S.; Bresser, D. ZnO-Based Conversion/Alloying Negative Electrodes for Lithium-Ion Batteries: Impact of Mixing Intimacy. *Energy Technol.* **2021**, *9*, 2001084. [CrossRef]

18. Birrozzi, A.; Asenbauer, J.; Ashton, T.E.; Groves, A.R.; Geiger, D.; Kaiser, U.; Darr, J.A.; Bresser, D. Tailoring the Charge/Discharge Potentials and Electrochemical Performance of SnO2 Lithium-Ion Anodes by Transition Metal Co-Doping. *Batter. Supercaps* **2020**, *3*, 284–292. [CrossRef]

19. Giuli, G.; Trapananti, A.; Mueller, F.; Bresser, D.; d'Acapito, F.; Passerini, S. Insights into the Effect of Iron and Cobalt Doping on the Structure of Nanosized ZnO_2. *Inorg. Chem.* **2015**, *54*, 9393–9400. [CrossRef]

20. Biesinger, M.C.; Payne, B.P.; Grosvenor, A.P.; Lau, L.W.M.; Gerson, A.R.; Smart, R.S.C. Resolving Surface Chemical States in XPS Analysis of First Row Transition Metals, Oxides and Hydroxides: Cr, Mn, Fe, Co and Ni. *Appl. Surf. Sci.* **2011**, *257*, 2717–2730. [CrossRef]

21. Briggs, D.; Wanger, C.D.; Riggs, W.M.; Davis, L.E.; Moulder, J.F.; Muilenberg, G.E. *Handbook of X-Ray Photoelectron Spectroscopy*; Perkin-Elmer Corp., Physical Electronics Division: Eden Prairie, MI, USA, 1981; Volume 3, p. 195. [CrossRef]

22. Huang, J.; Liu, Y.; Wu, Y.; Li, X. Influence of Mn Doping on the Sensing Properties of SnO_2 Nanobelt to Ethanol. *Am. J. Anal. Chem.* **2017**, *8*, 60–71. [CrossRef]

23. Tallapally, V.; Esteves, R.J.A.; Nahar, L.; Arachchige, I.U. Multivariate Synthesis of Tin Phosphide Nanoparticles: Temperature, Time, and Ligand Control of Size, Shape, and Crystal Structure. *Chem. Mater.* **2016**, *28*, 5406–5414. [CrossRef]

24. Li, J.-T.; Swiatowska, J.; Seyeux, A.; Huang, L.; Maurice, V.; Sun, S.-G.; Marcus, P. XPS and ToF-SIMS Study of Sn–Co Alloy Thin Films as Anode for Lithium Ion Battery. *J. Power Sources* **2010**, *195*, 8251–8257. [CrossRef]

25. Ehinon, K.K.D.; Naille, S.; Dedryvère, R.; Lippens, P.-E.; Jumas, J.-C.; Gonbeau, D. Ni3Sn4 Electrodes for Li-Ion Batteries: Li−Sn Alloying Process and Electrode/Electrolyte Interface Phenomena. *Chem. Mater.* **2008**, *20*, 5388–5398. [CrossRef]

26. Wen, C.J.; Huggins, R.A. Thermodynamic Study of the Lithium-Tin System. *J. Electrochem. Soc.* **1981**, *128*, 1181–1187. [CrossRef]

27. Huggins, R.A.; Wen, C.J. Chemical Diffusion in Intermediate Phase in the Lithium-Tin System. *J. Solid State Chem.* **1980**, *35*, 376–384.

28. Winter, M.; Besenhard, J.O. Electrochemical Lithiation of Tin and Tin-Based Intermetallics and Composites. *Electrochim. Acta* **1999**, *45*, 31–50. [CrossRef]

29. Goward, G.R.; Taylor, N.J.; Souza, D.C.S.; Nazar, L.F. The True Crystal Structure of Li17M4 (M=Ge, Sn, Pb)–Revised from Li22M5. *J. Alloys Compd.* **2001**, *329*, 82–91. [CrossRef]

30. Ma, Y.; Ulissi, U.; Bresser, D.; Ma, Y.; Ji, Y.; Passerini, S. Manganese Silicate Hollow Spheres Enclosed in Reduced Graphene Oxide as Anode for Lithium-Ion Batteries. *Electrochim. Acta* **2017**, *258*, 535–543. [CrossRef]

31. Darr, J.A.; Zhang, J.; Makwana, N.M.; Weng, X. Continuous Hydrothermal Synthesis of Inorganic Nanoparticles: Applications and Future Directions. *Chem. Rev.* **2017**, *117*, 11125–11238. [CrossRef]

32. Toby, B.H.; Von Dreele, R.B. GSAS-II: The Genesis of a Modern Open-Source All Purpose Crystallography Software Package. *J. Appl. Crystallogr.* **2013**, *46*, 544–549. [CrossRef]

33. Ravel, B.; Newville, M. ATHENA, ARTEMIS, HEPHAESTUS: Data Analysis for X-Ray Absorption Spectroscopy Using IFEFFIT. *J. Synchrot. Radiat.* **2005**, *12*, 537–541. [CrossRef]

34. Joly, Y. X-Ray Absorption near-edge Structure Calculations beyond the Muffin-Tin Approximation. *Phys. Rev. B Condens. Matter Mater. Phys.* **2001**, *63*, 125120. [CrossRef]

35. Hedin, L.; Lundqvist, B.I.; Lundqvist, S. Local Exchange-Correlation Potentials. *Solid State Commun.* **1971**, *9*, 537–541. [CrossRef]

36. Filipponi, A.; Di Cicco, A.; Natoli, C.R. X-Ray-Absorption Spectroscopy and n-Body Distribution Functions in Condensed Matter. I. Theory. *Phys. Rev. B* **1995**, *52*, 15122–15134. [CrossRef] [PubMed]

37. Filipponi, A.; Di Cicco, A. X-Ray-Absorption Spectroscopy and n-Body Distribution Functions in Condensed Matter. II. Data Analysis and Applications. *Phys. Rev. B* **1995**, *52*, 15135–15149. [CrossRef]

38. Giorgetti, M.; Mukerjee, S.; Passerini, S.; McBreen, J.; Smyrl, W.H. Evidence for Reversible Formation of Metallic Cu in Cu0.1V2O5 Xerogel Cathodes during Intercalation Cycling of Li+ Ions as Detected by X-ray Absorption Spectroscopy. *J. Electrochem. Soc.* **2001**, *148*, A768. [CrossRef]